





Nanoindentation of Supercrystalline Nanocomposites: Linear Relationship Between Elastic Modulus and Hardness

CONG YAN,¹ BÜSRA BOR,² ALEXANDER PLUNKETT,²
BERTA DOMÈNECH ², GEROLD A. SCHNEIDER,²
and DILETTA GIUNTINI ^{1,2,3}

1.—Department of Mechanical Engineering, Eindhoven University of Technology, Eindhoven, Netherlands. 2.—Institute of Advanced Ceramics, Hamburg University of Technology, Hamburg, Germany. 3.—e-mail: d.giuntini@tue.nl

Supercrystalline nanocomposites (SCNCs) are a new category of nanostructured materials, with organically functionalized nanoparticles assembled into periodic structures, reminiscent of atomic crystals. Thanks to this nanoarchitecture, SCNCs show great promise for functional applications, and understanding and controlling their mechanical properties becomes key. Nanoindentation is a powerful tool to assess the mechanical behavior of virtually any material, and it is particularly suitable for studies on nanostructured materials. While investigating SCNCs in nanoindentation, a linear proportionality has emerged between elastic modulus and hardness. This is not uncommon in nanoindentation studies, and here we compare and contrast the behavior of SCNCs with that of other material categories that share some of the key features of SCNCs: mineral-rich biocomposites (where mineral building blocks are packed into a protein-interfaced network), ultrafine grained materials (where the characteristic nano-grain sizes are analogous to those of the SCNC building blocks), and face-centered cubic atomic crystals (which share the typical SCNC periodic structure). A strong analogy emerges with biomaterials, both in terms of the hardness/elastic modulus relationship, and of the correlation between this ratio and the dissipative mechanisms occurring upon material deformation. Insights into the suitability of SCNCs as building blocks of the next-generation hierarchical materials are drawn.

Supercrystalline nanocomposites (SCNCs) are systems of self-assembled nanoparticles that are being thoroughly explored for both fundamental studies and their many potential applications.^{1,2} Generally consisting of organically functionalized metallic or ceramic nanoparticles (NPs), arranged into long-range order nanoarchitectures through self-assembly processes, they combine the unique features of nano-sized building blocks with the properties that arise from their periodic arrangement. These aspects make them an ideal platform

for studies on the interaction and behavior of materials made of periodically arranged building blocks, with both interesting parallelisms and contrasts with crystalline materials.³ Additionally, their so-called emergent collective properties, arising from the presence of these same self-organized nanostructures, have been identified as promising for applications in a variety of fields: catalysis, energy storage, biomedical products, drug delivery, optoelectronics, magnetic devices, and more.^{2,4,5}

One aspect of SCNCs' behavior that is often only superficially explored, however, is the set of their mechanical properties. These are, nonetheless, features that need to be understood and controlled to allow the use of SCNCs in most of the applications listed above.^{6–9} Our group has been exploring the mechanical behavior of these materials in detail, with analyses of their strength, stiffness, and

(Received December 21, 2021; accepted March 25, 2022; published online April 15, 2022)

hardness under multiple loading conditions, and through both ex- and in-situ studies.^{10–16} Important findings in this regard are the remarkable boost in strength, hardness, toughness, and stiffness enabled through the crosslinking of the organic ligands that functionalize and interface with the NPs, and the ability of supercrystals to deform according to patterns analogous to the ones observed in atomic crystals, such as dislocations, pile-ups, and slip bands.^{3,10,11,15}

Even though these micromechanical studies are instrumental to reveal the multifaceted aspects of the constitutive behavior of such unconventional nanostructured materials, an important tool to measure the mechanical properties of SCNCs is nanoindentation.^{11,17} Nanoindentation is a versatile technique to assess the nano- and micro-scale mechanical properties of a multiplicity of materials. It has two major advantages with respect to other micromechanical tests: its simplicity of implementation and, in contrast for example to microcompression and microbending, the absence of the potential material alterations induced by the focused ion beam (FIB).^{16–18} For SCNCs, nanoindentation is typically the tool of choice for mechanical studies, especially since in most cases they are produced in small sizes, ranging up to tens of micrometers.^{8,11} Even though steps forward have been made towards processing bulk macroscopic supercrystals,^{5,10,19} nano-indentation remains an effective and efficient tool for the assessment of these properties.

The mechanical properties that are most commonly measured via nanoindentation are the material's Young's modulus (E) and hardness (H).^{17,18} E is in most cases assessed through the so-called continuous stiffness method (CSM).^{20,21} During CSM the loading ramp of the nanoindentation cycle is performed via a sequence of very small loading-unloading steps, and it is from this sequence of unloading steps that the Young's modulus is calculated. This leads to higher reliability with respect to measuring E only at one instance, at the start of the overall nanoindentation cycle's unloading, which can often be affected by time-dependent phenomena (e.g., creep). H , on the other hand, is calculated based on the applied indentation load and the projected area of the resulting imprint, taking care to consider the effects of pile-ups and sink-ins.¹¹

E is relative to the purely elastic behavior of a material, while H accounts for both elastic and plastic effects, i.e., recoverable and permanent deformation, respectively. Defining a relation between the two, analytical or empirical, has been a long-standing challenge in the materials science and nano/micromechanics communities.^{20,22–25} Beyond the fundamental interest in capturing such an inter-relation, a predictive model to deduce H from E would also be valuable to obviate an issue affecting the majority of nanoindentation hardness data, the so-called indentation size effect (ISE).²⁶

When the ISE occurs, the measured H increases with reducing indentation depth. Above a certain indentation depth (usually in the μm range), H reaches an asymptotic value. However, for many nanostructured and nanoarchitected materials, there is an interest in probing mechanical properties at depths shallower than $1\ \mu\text{m}$,¹¹ which is where a reliable relationship between E and H becomes particularly valuable.

In the quest towards such a relationship, an interesting trend has emerged in a variety of materials categories: nanoindentation E and H are often found to be linearly proportional to each other. This is not an obvious phenomenon, especially since it spans many different materials types, and because hardness can correlate to a material's resistance against multiple types of deformation (penetration, scratch), while accounting for both reversible (elastic) and irreversible phenomena. The linearity of the H/E relationship has nevertheless been detected in a diverse set of materials: ceramics, intermetallics, metallic glasses, biocomposites, and molecular crystals.^{22,24,27,28} More recently, the same trend has emerged for SCNCs, as will be shown in detail in the following.

Beyond the more qualitative explanations for this linearity, based on considerations of the strength of chemical bonds and the respective correlations between hardness, yield strength, and elastic modulus, some quantitative models have been proposed. In one of the first models, Gilman correlated H with the bulk modulus B , even though focusing on covalent crystals.²⁹ A more general relationship was later proposed by Teter, linking empirically H and shear modulus, G .²⁵ Recently, an analytical model has confirmed such a linear relationship between hardness and shear modulus for the case of Vickers hardness, even though a more accurate correction, still analytical, has been proposed based on the Pugh's ratio, to account for the presence of some amount of plastic deformation. This resulted in capturing well the behavior of intermetallics and bulk metallic glasses.²²

More in general, since H accounts for resistance to both reversible and irreversible deformations, while E accounts for reversible phenomena only, the H/E ratio has become a tool to account for the relative importance of these two types of phenomena, especially when elasto-plasticity dominates the constitutive response of a material. The H/E ratio then also becomes correlated with the damage mechanisms underlying brittle and plastic failure.³⁰

In the following, we explore the relationship between E and H for SCNCs, and we rationalize it based on the available models, and through a compare-and-contrast analysis with other relevant material categories. More specifically, we compare the case of SCNCs with other material systems that share at least one of the SCNC's distinguishing features. These are:

(1) mineral-organic biocomposites that are mineral-rich (which, like SCNCs, consist of nano-sized mineral building blocks interfaced by an ultra-thin organic layer); (2) ultrafine-grained materials, UFGs (which share the characteristic sub-micron size of their building blocks, drawing an analogy between grain boundaries and the typically nanometer to sub-nanometer organic layer in between NPs in SCNCs); and (3) single (atomic) crystals with an FCC (face-centered cubic) lattice, which is also the most common arrangement of NPs in SCNCs, even though at a scale that is two orders of magnitude larger than in atomic crystals. The first material category, highly mineralized biocomposites, share a similar composition to SCNCs; UFG materials share the nano-size of the building blocks; while FCC single crystals share the arrangement of such building blocks. Additional material categories showing this linear E/H relationship are also considered.

The SCNCs that we have been using as a model system in most mechanical studies consist of iron oxide NPs (mainly magnetite, Fe_3O_4) with a diameter in the 14–19 nm size range. These are surface-functionalized with organic ligands, most often with oleic acid, OA ($\text{C}_{18}\text{H}_{34}\text{O}_2$), but in several cases with oleyl-phosphate, OPh ($\text{C}_{18}\text{H}_{37}\text{O}_4\text{P}$), so that they are colloidally stable when dispersed in an organic solvent (e.g., toluene, chloroform, dichloromethane). Both these ligands consist of aliphatic chains with a double carbon-carbon bond ($\text{C}=\text{C}$), and differ only in the anchoring group to the particle surface. Self-assembly is then carried out either via evaporation of the solvent, or solvent-destabilization through the diffusion of a non-solvent (e.g., ethanol).^{11,12} The self-assembly results in the formation of the supercrystalline nanostructure (also called superlattice). All details on the starting material's nano-building blocks and the self-assembly routines are detailed in previous works.^{10–13,15,16}

While in most cases SCNCs are produced in the form of thin films or micron-sized three-dimensional materials,¹ the procedure developed in our group leads to bulk, centimeter-sized supercrystalline pellets.^{10,11} This entails the presence of the same variety of defects affecting crystalline materials (point, line, surface/interface, and volume defects), and thus the poly-supercrystalline nature of the nanocomposites.³ We are thus dealing with hierarchical materials, made of nanocrystals (the NPs are mostly single crystals), interfaced by anchored and confined organic ligands (in inter-particle spacings ranging between 0.5 and 2 nm), and organized into supercrystalline domains (up to tens of micrometers in size), which compose the macroscale pellets. Since nanindentation probes multiple different supercrystalline orientations in the material, the measured properties can be considered isotropic. This is generally considered valid also in the case of many

hierarchical biocomposites, and for FCC-structured materials, since FCC arrangements are the lattice type that is the closest to being isotropic.^{10,30}

A key step in strengthening, stiffening, hardening, and toughening the SCNCs has been found in crosslinking the NP-interfacing organic ligands. Crosslinking can be induced via heat treatment at mild temperatures—up to 350°C, above which the ligands start decomposing and the ultra-high surface area of the NPs leads to sintering.^{5,10,15,16} At lower temperatures, instead, this step leads to the formation of covalent bonds between adjacent organic chains, shifting the interactions that hold the SCNCs together from van der Waals-dominated to strong chemical bonds. Since the ligands are anchored to the NP surfaces, and the crosslinking creates a covalent network throughout all NP-NP interfaces, a mechanical properties boost is obtained. In some cases, before heat treatment, the self-assembled nanocomposites are uniaxially pressed in a rigid die at 150°C, to shape them into cylindrical pellets that can be more easily handled.¹¹

Nanindentation data relative to the iron oxide-OA and iron oxide-OPh supercrystalline materials were obtained via the CSM method using an Agilent Nano Indenter G200 (Agilent, Santa Clara, CA, USA), with a Berkovich tip and with an indentation depth of 300 nm, chosen to allow probing the bulk properties of the nanocomposites without inducing cracking.¹¹ It is worth mentioning here that through a previous nanindentation campaign, it has emerged that the non-crosslinked SCNCs are not affected by the indentation size effect (ISE), since in this state the material can be more easily compacted, while for crosslinked materials both E and H decrease with increasing indentation depth, due to cracking starting at depths higher than 300 nm.¹¹

The measured E and H values obtained for OA- and OPh-based iron oxide supercrystals, processed with varying crosslinking-inducing temperatures, are shown in Fig. 1a. Here, data is shown for materials just self-assembled and pressed (as-pressed, AP), and heat-treated (HT) at 250, 325, and 350°C. The linear proportionality between E and H appears evident, independently of the ligand type, processing stage, and heat treatment temperature. It is worth highlighting explicitly the very high values of both elastic modulus and hardness (up to 60 and 6 GPa, respectively) for materials the building blocks of which are mainly held together by an organic network.¹⁵

To verify whether this linear proportionality between H and E is also common to a wider spectrum of SCNCs, in Fig. 1b we gathered the data on our SCNCs prior to crosslinking, with data on other analogous self-assembled materials from the literature. These additional SCNCs span both different types of NPs (for composition, shape, and size) and organic ligands.^{8,9,31–33} All details on the

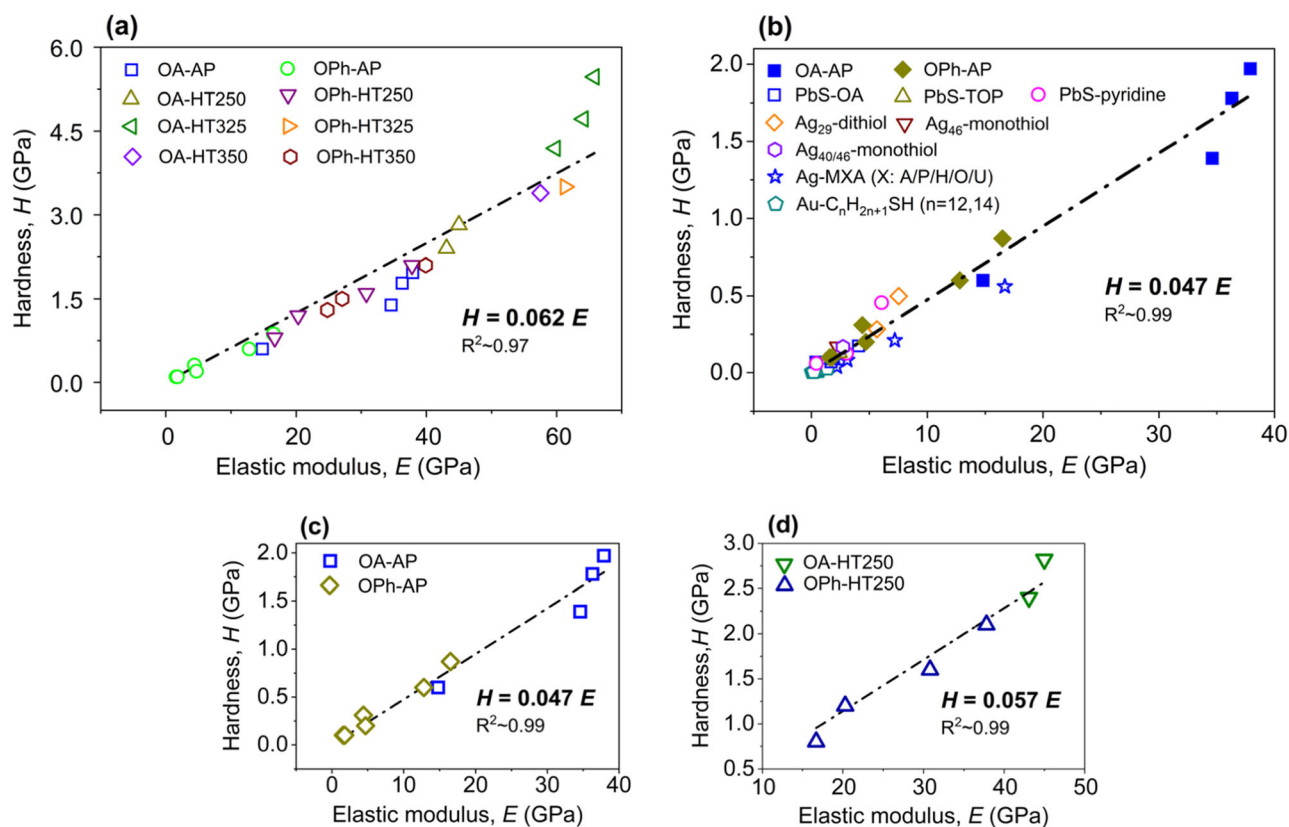


Fig. 1. Nanoindentation hardness (H) and elastic modulus (E) of supercrystalline nanocomposites (SCNCs), for: (a) bulk iron oxide-oleic acid (OA) and iron oxide-oleyl phosphate (OPh) SCNCs, measured after pressing (AP), and heat treatment at 250, 325, and 350°C; (b) bulk iron oxide-oleic acid (OA) and iron oxide-oleyl phosphate (OPh) SCNCs, measured after pressing (AP) compared with data relative to other SCNCs from the literature (with varying organic ligands, NP size, shape, and material);^{8,9,31–33} (c–d) bulk iron oxide-oleic acid (OA) and iron oxide-oleyl phosphate (OPh) SCNCs non-heat-treated (not crosslinked, c), crosslinked at 250°C (d).^{10,11,41,42}

literature data are given in Table I of the Appendix. Note that here we only consider the data on OA- and OPh-based SCNCs in the as-pressed (AP) state, since the other supercrystals reported on in the literature are not crosslinked. Remarkably, an alignment between all data points is observed, indicating that the linear H/E trend is common to a broad spectrum of such materials, independently of their composition.

Interestingly, if we distinguish the data based on the crosslinking temperature (AP and 250°C), as shown in Fig. 1c, d, the slope of the linear fit of H data with respect to E changes, tending to increase with heat treatment temperature. This trend is also currently being confirmed for the 325°C case, for which preliminary data show $H/E \sim 0.071$. This implies a shift in the ratio of irreversible to reversible deformations occurring upon nanoindentation. The change in the governing interactions between the SCNCs' building blocks (from weak, van der Waals-dominated, to covalent bonds) thus appears to play a more significant role in altering the H/E relationship, compared with the specific material composition. More data is being collected to verify this effect. One can also notice that the

slope of the non-crosslinked materials (Fig. 1b, c) is very similar to the case of molecular crystals,²⁸ which are held together by weak interactions too.

Based on these observations, we compared the relationship obtained for SCNCs, $H/E = 0.062$, with another material category characterized by a similar composition. We thus looked into high-mineral content biomaterials, which consist of a high volume-fraction of inorganic (mineral) nano-building blocks interfaced by an ultra-thin layer of confined organics (organic content in the 1–15 wt.% range, while for SCNCs the range is typically 2–10 wt.%). Indeed, the linear H vs E relationship for biomaterials has recently been explored by Labonte and coworkers, who found the same kind of trend.³⁰ This appeared to be consistent within a variety of biological materials. We focus here on materials with high mineral content, see Fig. 2, and we observe linearity with a slope analogous to that relative to SCNCs, and values of E and H going beyond supercrystals, up to twice the values relative to crosslinked ones (140 and 12 GPa, respectively—see Table II in the Appendix for details on the literature data). Note that some of the data reported in Fig. 2 were obtained with a cube-corner

tip instead of a Berkovich one (as marked in the figure), and it was thus rescaled into a Berkovich indentation hardness.³⁰

The next feature that we considered was the characteristic nanostructure scale of SCNCs, meaning the presence of building blocks with sub-micron characteristic size (note that this is also often typical of the biomaterials considered above). We thus include in the analysis UFG ceramics and metallic materials (pure metals and alloys). The respective nanoindentation data are shown in Fig. 3a, b (see Table III in the Appendix). The linear trend appears to be less sharp here, for both cases. UFG ceramics typically show more potential for nonlinear irreversible deformation than their coun-

terparts with larger grain sizes,³⁴ and metallic materials are well known to deform plastically, even in their UFG form, which can lead to strengthening and somewhat reduced ductility.³⁵ Since the linear proportionality between E and H is typically detected in, and rationalized for, materials having a dominantly elastic behavior under loading, the deviations from linearity for UFG materials can be attributed to this factor.²² Additional phenomena can also play a role, such as microcracking and strain delocalization. Indeed, even though SCNCs can reach values of fracture toughness indicating the presence of extrinsic toughening mechanisms,^{11,16} their constitutive behavior in compression and bending is largely linear elastic.¹⁶ Especially after crosslinking, the covalently bonded organic network is likely behaving in a brittle manner, while toughening is expected to arise from viscous dissipation and crack path deviation within the organic fractions of the superlattice. It thus appears that the similarity between biocomposites and SCNCs in terms of H/E relationship relies on their comparable compositions, while the nano-size of the material building blocks does not seem to necessarily lead to a linear relationship between nanoindentation modulus and hardness.

We then looked into the nanostructural arrangement parameter, and more specifically the periodic arrangement of the NPs in the superlattice. Since SCNCs most often feature FCC long-range order, we considered nanoindentation data relative to single atomic crystals with this same lattice type. It was found that these show an even less linear H/E trend, see Fig. 4 and the respective Table IV in the Appendix. The H/E ratio values appear to vary with the tested material, but not the tested crystallographic orientation. The three data points relative to different crystallographic directions in Al overlap,³⁶ while the data points relative to the (001) direction in different materials (Ni, Ag, Au)^{37,38} show different H/E values. Note also that the

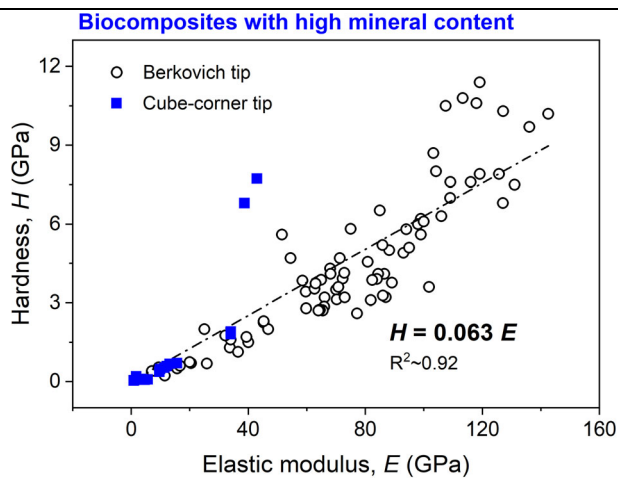


Fig. 2. Nanoindentation hardness (H) and elastic modulus (E) for biocomposites with high mineral content.⁴³⁻⁶⁹ These biocomposites share the composition as SCNCs, with mineral (ceramic) building blocks interfaced by an ultra-thin organic layer. The pictured data are mainly obtained via a Berkovich tip, while some indents were performed with a cube-corner tip (marked by blue squares), and are here rescaled to a Berkovich indentation hardness (Color figure online).

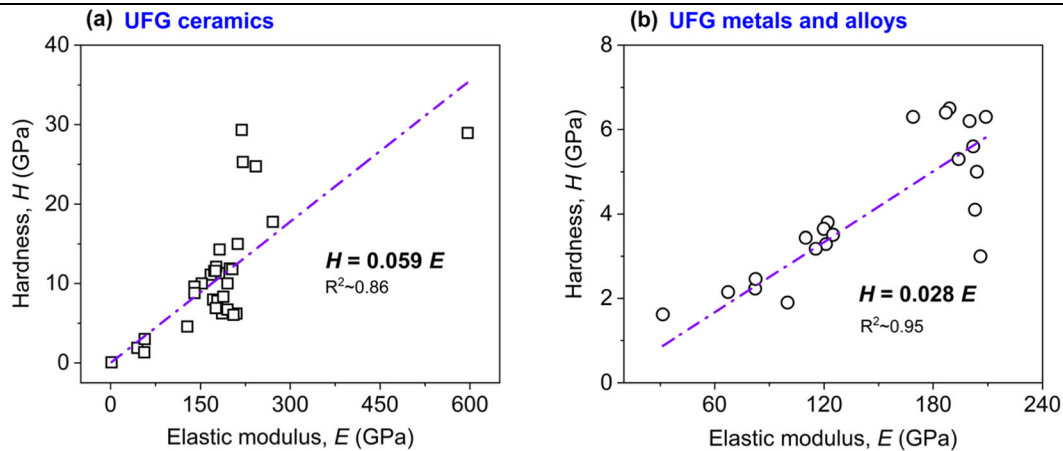


Fig. 3. Nanoindentation hardness (H) and elastic modulus (E) for UFG materials: (a) ceramics; (b) metals and alloys.⁷⁰⁻⁸⁷ UFG materials share the characteristic sub-micron building block size of SCNCs.

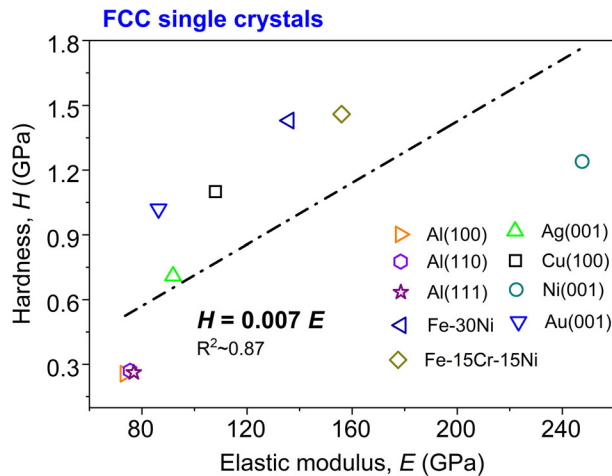


Fig. 4. Nanoindentation hardness (H) and elastic modulus (E) for single (atomic) crystals with face-centered cubic lattice (FCC).^{36–38,88} SCNCs also typically show an FCC arrangement of the constituent NPs, even at a scale two orders of magnitude larger than in atomic crystals.

Fe-Cr-Ni alloys can feature both BCC and FCC lattices, the data shown here are relative to single FCC crystals only.

As mentioned above, the elastic anisotropy in FCC structures is indeed not severe, and H has also been shown to vary with changing crystallographic orientations.³⁶ As for comparing different materials, even though FCC single crystals all share the same slip system ($\{111\}\langle 110\rangle$), their yield strength varies, since each material has a different shear stress required to activate dislocations (and thus plasticity). The H/E ratio can be regarded as an indicator of the predominance of reversible over irreversible deformation, and plasticity is an irreversible phenomenon. In FCC metals with lower yield strength, then, plastic deformation dominates the response to nanoindentation, thus leading to lower H/E values. In general, thanks to the absence of grain boundaries and their tightly packed atomic arrangement, single FCC crystals are extremely ductile. Therefore, the deviation from the linear proportionality between H and E is likely connected to the important role that inelastic deformation phenomena (and specifically slip) play during indentation.

In line with these considerations, amorphous materials like bulk metallic glasses (BMGs) and amorphous silicon show, instead, a clear linear proportionality between E and H , see Fig. 5 (and Table V in the Appendix). These are materials that mainly show limited ductility (even though shear phenomena are detected upon indentation), and thus also suggest that the periodic arrangement of

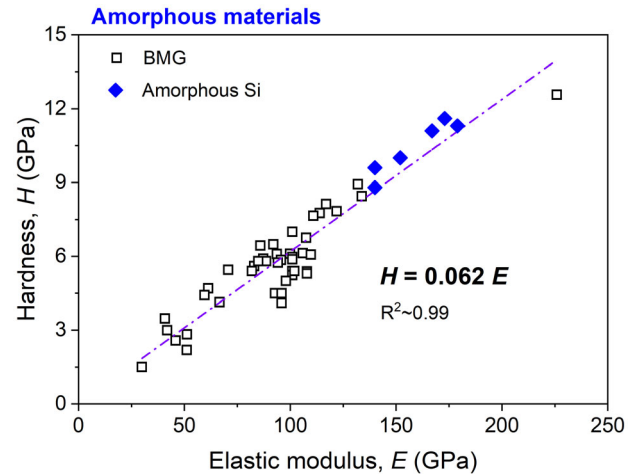


Fig. 5. Nanoindentation hardness (H) and elastic modulus (E) of amorphous materials—bulk metallic glasses (BMGs) and non-crystalline silicon.^{39,76,89–94}

elementary building blocks is not instrumental in a linear proportionality between nanoindentation elastic modulus and hardness.

For the materials for which the linear H/E relationship holds, i.e., those with limited ability to deform via irreversible mechanisms, models able to capture the proportionality between nanoindentation hardness and modulus have been proposed. Chen et al. have analytically shown, starting from the definition of Vickers hardness, that

$$H = 0.151G \quad (1)$$

with $G = E/[2(1+\nu)]$ being the shear modulus, and ν the Poisson's ratio.²² Note that Vickers and Berkovich hardness data are directly comparable. This relationship relies on the assumption of isotropic and homogeneous material behavior which, as discussed above, can be considered applicable to the materials studied here. Given the Poisson's ratio of SCNCs, 0.34, calculated via numerical simulations for crosslinked materials and here extrapolated to the non-crosslinked case too,¹³ a good agreement between the supercrystalline materials data and this model is found: for SCNCs, according to this model we find $H = 0.056$, while by fitting the data shown in Fig. 1a, one finds $H = 0.062 E$.

The H/E ratio also suggests a similarity between SCNCs and biocomposites. Based on the fitting of experimental data, H/E is 0.062 in both cases. For UFG ceramics this value is 0.059, even if in that case the linear fit is not as accurate (Fig. 3a). The ratio's value then progressively decreases when moving to molecular crystals (0.043), UFG metals and alloys (0.028), and FCC single crystalline

metals (0.007). A trend appears, with H/E decreasing with increasing ductility of the materials in question, as depicted in Fig. 6. This is in line with the physical meaning that is associated with the ratio between nanoindentation hardness and Young’s modulus, as described in the following.

There is a general agreement in considering the H/E ratio to be itself linearly proportional to the energy dissipated during the nanoindentation loading-unloading cycle.^{23,24,30} More specifically, H/E is proportional to the ratio of W_u , the work applied by the material on the indenter’s tip upon unloading, over W_t , the total nanoindentation work. W_u is commonly considered to represent a good estimation of the elastic part of the energy associated with the nanoindentation cycle, since the recoverable deformation is detected only during unloading. W_u does not correspond exactly to the elastic work if residual stresses are present, but in this context we consider this mismatch to be negligible.²⁴

It has then been shown that

$$\frac{H}{E} \bigg/ \frac{W_u}{W_t} = \frac{2}{3(1+\nu)} \cot\alpha \quad (2)$$

where α is the indenter’s half-angle. While confirming the linear proportionality between H and E modeled by Eq. (1), this relationship additionally relates the constant of proportionality between hardness and modulus to the ratio between the energy dissipated during nanoindentation via reversible and irreversible deformation mechanisms. The smaller H/E is, the smaller W_u/W_t becomes. Decreasing values of W_u/W_t indicate that irreversible deformation mechanisms prevail over the reversible (mainly elastic) ones. With increasing H/E ,

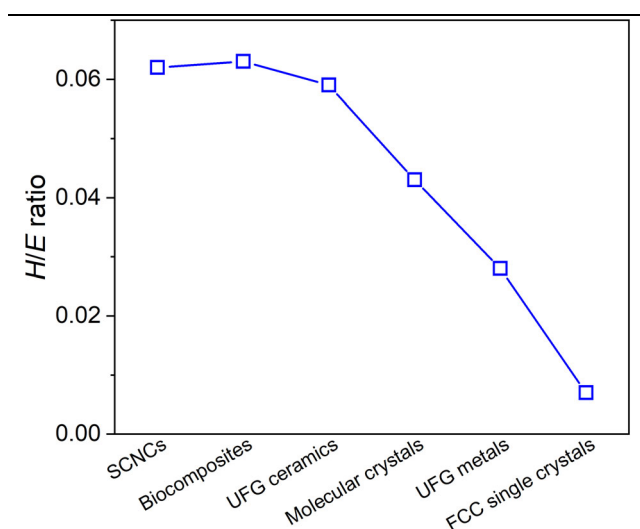


Fig. 6. The ratio between nanoindentation hardness (H) and elastic modulus (E) for SCNCs and the material categories considered for comparison (highly mineralized biocomposites, UFG ceramics and metals, molecular crystals, and single crystals with face-centered cubic atomic lattice).^{39,76,89–94}

E , then, the material’s mechanical behavior tends to become fully elastic, and thus lacks the ability to deform irreversibly prior to failure.

This same concept has been rationalized by Labonte and coworkers (in the context of biological materials) with the introduction of the variable $I_E = H/E$, defined as “elasticity index,” or resistance to irreversible deformation.³⁰ The higher I_E , the more dominant reversible (elastic) deformation is. Materials with higher values of H/E tend, indeed, to show a less ductile behavior compared with those featuring lower values, in line with the experimental data shown above (Figs. 2–6). When I_E instead tends to zero, irreversible deformation dominates the mechanisms underlying a material’s hardness.

We therefore analyzed the relationship between H/E and W_u/W_t for SCNCs, based on the nanoindentation data available for the iron oxide-OA and -OPh systems, heat-treated at different temperatures. As shown in Fig. 7, the expected linear trend is found, with a proportionality of 0.205. This is in reasonable agreement with the value calculated with Eq. 2, given the half-angle of the Berkovich indenter (65.27°) and the same Poisson’s ratio value of 0.34, resulting in 0.229. The slight discrepancy is attributed to the presence of time-dependent deformations (viscoelastic and viscoplastic), which are generally associated with the presence of an organic phase in the nanocomposites.¹⁶

The models describing the relationship between E and H in nanoindentation [Eqs. 1 and 2] are thus applicable to supercrystalline nanocomposites, since SCNCs are also characterized by limited ductility, as the relatively high value of the H/E ratio confirms. On the other hand, SCNCs feature levels of fracture toughness up to $0.5 \text{ MPa} \sqrt{\text{m}}$ in first fracture mode (crack opening), and similar values also for the second fracture mode (crack sliding).^{11,16} These are significantly higher (one order of magnitude) than the values that would be expected in the

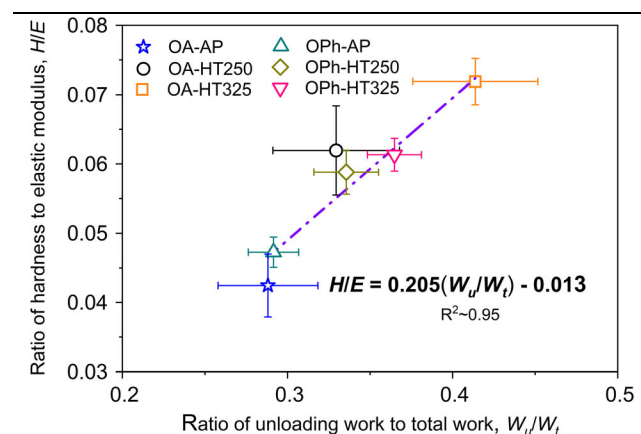


Fig. 7. Nanoindentation hardness to elastic modulus ratio (H/E) for iron oxide-based supercrystalline nanocomposites (SCNCs) with oleic acid and oleyl-phosphate as organic ligands, plotted as a function of the ratio of unloading work to the total indentation work.

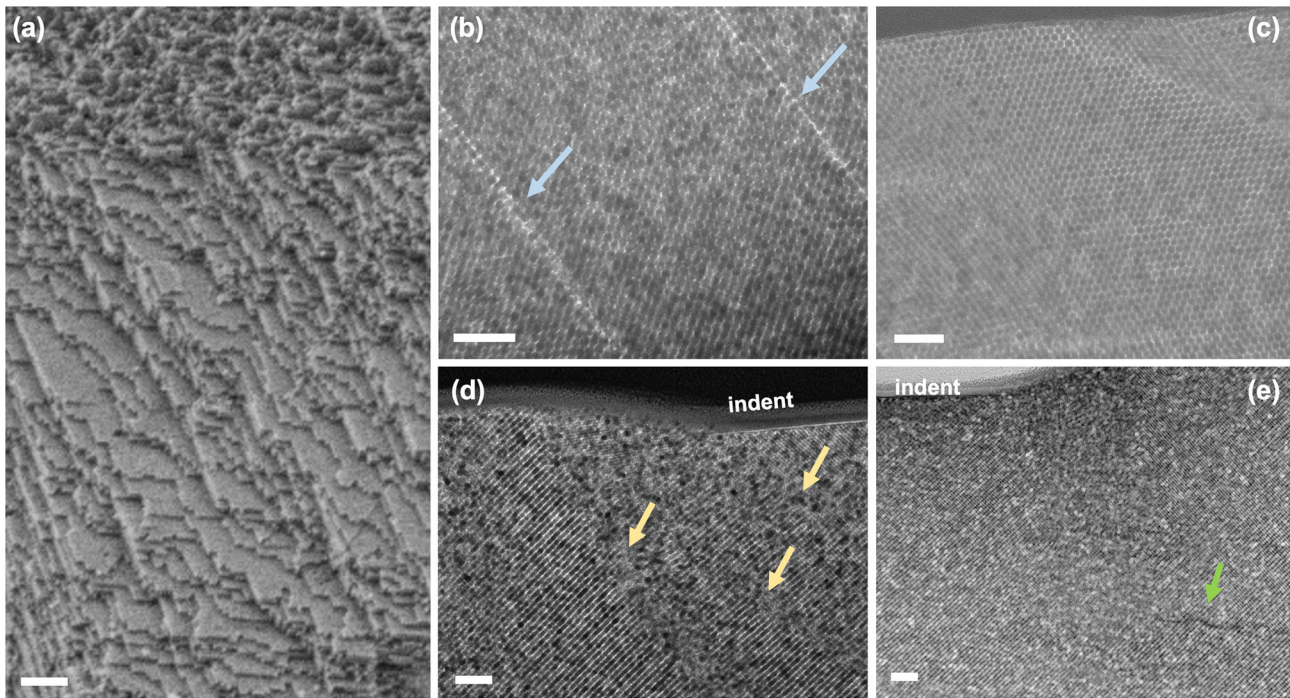


Fig. 8. Superlattice structure and nanoindentation-induced deformations in SCNCs: (a) unperturbed supercrystalline lattice in OPh-based nanocomposite heat-treated at 325°C; (b) slip bands detected under 500-nm-deep indent in AP (not heat-treated) OA-based SCNC; (c) pile-up around 500-nm-deep indent in AP OA-based SCNC; (d) sub-indent compressed and deformed area in OA-based SCNC heat-treated at 325°C; (e) localized damage under indent in HT-325°C OA-based SCNC. (a) is an SEM micrograph, (b–d) are TEM micrographs, (e) is a STEM high-angle annular dark field micrograph. Scale bars are 200 nm in (a), 100 nm in (b–e). For additional details see³.

case of only intrinsic mechanisms occurring around the crack, according to an estimation based on the Barenblatt model.¹¹

The same holds, again, for biomaterials, especially those with high mineral content: we have shown above that they have an H/E ratio comparable to the SCNC case, even though they are well known to reach remarkable values of toughness. Biological materials have, in fact, become a source of material design inspiration for toughening materials that are intrinsically brittle, such as ceramics.^{10,39}

For both biocomposites and SCNCs, a key role towards toughening is likely played by quasi-plastic phenomena. These are irreversible deformation mechanisms that are not properly associated with ductility, yet responsible for energy dissipation and thus toughening effects. Examples are strain delocalization via microcracking, sliding of nano/micro-sized building blocks, and distributed shear faults. These have consistently been observed in biomaterials, and lately also in SCNCs, both in the presence and absence of crosslinking of the organic

ligands.^{3,40} The transmission electron micrographs in Fig. 8 show some examples of slip bands and dislocation-like structures under indents in SCNCs.

These multiple analogies between SCNCs and biological materials are particularly interesting from the perspective offered by the field of biomimetics. Supercrystalline nanocomposites have gained growing attention not only thanks to their multiple promising functional applications, but also for their suitability as building blocks for hierarchical ceramic-based composites with enhanced fracture toughness.^{41,42} With their tightly packed superlattices (and especially in presence of organic crosslinking) they do not compromise strength, hardness, or stiffness, while offering the opportunity for toughening. This occurs through crack deviation within their confined organic phase, but also, even more importantly, when supercrystalline micro-sized building blocks are embedded in another soft organic matrix.

It is worth mentioning the connection with nacre here (mother of pearl), the most typical inspiration for the development of tough ceramics thanks to its

characteristic brick-and-mortar structure.⁹⁵ The bricks constituting nacre are themselves nanocomposites, made of mineral nanocrystals interfaced by an ultra-thin layer of protein material, of which SCNCs represent a strong analogy.^{2,27} We have shown here that the parallelisms between SCNCs and biocomposites reach into these materials' behavior when subjected to nanoindentation. A linear proportionality between E and H consistently emerges in both cases, with very comparable values of H/E ratios. This variable, an indication of the prevalence of reversible deformation mechanisms during loading, reaches quite high values, as expected when a material's constitutive behavior shows reduced ductility. On the other hand, the good levels of fracture toughness that SCNCs have been shown to reach, are likely due to quasi-plastic phenomena, which are also characteristic of biocomposites. Upon optimization of processing routines for the production of multiscale composites, we expect these kinds of nanostructured hybrid materials to become even more widespread, as building blocks for multifunctional components with enhanced mechanical properties.

ACKNOWLEDGEMENTS

The authors gratefully acknowledge the valuable support of Dr. Tobias Krekeler, Dr. Gunnar Schaan, and Dr. Martin Ritter (Central Electron Microscopy, BeEM, TUHH) for the TEM micrographs acquisition. The authors acknowledge support from the

Deutsche Forschungs-gemeinschaft (DFG, German Research Foundation), project numbers 192346071-SFB 986 and GI 1471/1-1.

CONFLICT OF INTEREST

The authors declare that they have no conflicts of interest.

OPEN ACCESS

This article is licensed under a Creative Commons Attribution 4.0 International License, which permits use, sharing, adaptation, distribution and reproduction in any medium or format, as long as you give appropriate credit to the original author(s) and the source, provide a link to the Creative Commons licence, and indicate if changes were made. The images or other third party material in this article are included in the article's Creative Commons licence, unless indicated otherwise in a credit line to the material. If material is not included in the article's Creative Commons licence and your intended use is not permitted by statutory regulation or exceeds the permitted use, you will need to obtain permission directly from the copyright holder. To view a copy of this licence, visit <http://creativecommons.org/licenses/by/4.0/>.

APPENDIX

See Tables I, II, III, IV and V.

Table I. Elastic modulus (E) and hardness (H) of supercrystalline nanocomposites (SCNCs), as shown in Fig. 1

Material	Size (nm)	E (GPa)	H (GPa)	Ref
PbS-OA	7	1.7	0.07	8
PbS-OA	4.7	0.4	0.068	9
PbS-OA	7.1	1.74	0.09	9
PbS-OA	13	4.07	0.174	9
PbS-pyridine	4.7	0.43	0.06	9
PbS-pyridine	7.1	3.04	0.125	9
PbS-pyridine	13	6.06	0.456	9
PbS-TOP	7.1	2.4	0.129	9
Ag-MAA		2.1	0.086	31
Ag-MPA		16.7	0.56	31
Ag-MHA		7.2	0.21	31
Ag-MOA		2.2	0.037	31
Ag-MUA		3.1	0.081	31
Au ₅ -C ₁₂ H ₂₅ SH	5	0.465	0.01	32
Au ₅ -C ₁₂ H ₂₅ SH	5	0.385	0.009	32
Au ₅ -C ₁₂ H ₂₅ SH	5	0.658	0.011	32
Au ₅ -C ₁₄ H ₂₉ SH	5	1.538	0.06	32
Au ₅ -C ₁₄ H ₂₉ SH	5	0.546	0.016	32
Au ₅ -C ₁₄ H ₂₉ SH	5	0.666	0.026	32
Au ₇ -C ₁₂ H ₂₅ SH	7	0.063	0.004	32
Au ₇ -C ₁₂ H ₂₅ SH	7	0.13	0.006	32
Au ₇ -C ₁₂ H ₂₅ SH	7	0.08	0.005	32
Au ₇ -C ₁₄ H ₂₉ SH	7	1.389	0.027	32
Au ₇ -C ₁₄ H ₂₉ SH	7	0.235	0.008	32
Au ₇ -C ₁₄ H ₂₉ SH	7	0.216	0.005	32
Ag ₂₉ -dithiol		5.66	0.2822	33
Ag ₂₉ -dithiol		7.53	0.4982	33
Ag ₄₆ -monothiol		2.27	0.1681	33
Ag _{40/46} -monothiol		2.73	0.1667	33

Table II. Elastic modulus (E) and hardness (H) of biomaterials with high mineral content, as shown in Fig. 2

Species	Part	E (GPa)	H (GPa)	Ref
<i>Lamprotula fibrosa</i>	Shell	59.66	3.42	43
<i>Cherax quadricarinatus</i>	Mandible	80.8	4.56	44
<i>Sphyrna tiburo</i>	Tooth	62.68	3.53	45
<i>Carcharias taurus</i>	Tooth	66.08	3.2	45
<i>Paracentrotus lividus</i>	Tooth	71.3	4.7	46
<i>Paracentrotus lividus</i>	Jaw	68	4.3	46
<i>Paracentrotus lividus</i>	Tooth	54.5	4.7	46
<i>Atrina pectinata</i>	Prismatic layers	59.8	2.79	47
Freshwater mussel	Prismatic layers	72.3	3.92	47
Human	Premolar	89.07	3.76	48
Human	Premolar	87.02	3.21	48
<i>Coscinodiscus</i> sp.	Frustule cribellum	3.4	0.076	49
<i>Coscinodiscus</i> sp.	Frustule cribrum	1.7	0.13	49
<i>Coscinodiscus</i> sp.	Frustule internal plate	15.61	0.53	49
<i>Coscinodiscus</i> sp.	Frustule gridle bands	4	0.059	49
<i>Novocrania anomala</i>	Dorsal valves	70	3.5	50
<i>Terebratulina retusa</i>	Dorsal valves	40	1.5	50
<i>Cryptochiton stelleri</i>	Teeth (magnetite veneer)	107.5	10.5	51
<i>Cryptochiton stelleri</i>	Teeth (core)	25	2	51
<i>Serraslmus manuely</i>	Tooth	86.5	4.1	52
<i>Serraslmus manuely</i>	Tooth	81.9	3.1	52
<i>Carcharodon carcharis</i>	Tooth	84.4	4.1	52
<i>Carcharodon carcharis</i>	Tooth	77.2	2.6	52
<i>Arapaima gigas</i>	Scale (external)	33.7	1.3	52
<i>Arapaima gigas</i>	Scale (internal)	15.7	0.5	52
<i>Atractosteus spatula</i>	Scale (external)	70.8	3.6	52
<i>Atractosteus spatula</i>	Scale (internal)	20.5	0.7	52
<i>Mergerlia truncata</i>	Shell (hinge)	72.82	4.14	53
<i>Mergerlia truncata</i>	Shell (commissure)	64.91	3.87	53
<i>Mergerlia truncata</i>	Shell (center)	70.24	3.12	53
<i>Mergerlia truncata</i>	Shell (dorsal valve)	65.94	2.85	53
<i>Mergerlia truncata</i>	Shell (ventral valve)	68.15	4.1	53
<i>Discradisca stella</i>	Shell (mineralized layer)	45.28	2.25	53
<i>Discradisca stella</i>	Shell (organic-rich layer)	7.07	0.4	53
<i>Discradisca stella</i>	Shell (Basal Plate)	39.37	1.7	53
<i>Lingula anatina</i>	Shell (mineralized layer)	34.03	1.6	53
<i>Lingula anatina</i>	Shell (organic-rich layer)	9.36	0.54	53
<i>Arapaima gigas</i>	Scale	46.8	2	54
<i>Arapaima gigas</i>	Scale	16.7	0.6	54
<i>Strombus gigas</i>	Shell	84	3.9	69
<i>Strombus gigas</i>	Shell	99	5.6	69
<i>Strombus gigas</i>	Shell	93	4.9	69
<i>Strombus gigas</i>	Shell	95	5.1	69
<i>Trochus niloticus</i>	Inner layer of shells (Nacre)	101.8	3.6	55
<i>Trochus niloticus</i>	Inner layer of shells (Nacre)	119.1	7.9	55
<i>Trochus niloticus</i>	Inner layer of shells (Nacre)	125.7	7.9	55
<i>Trochus niloticus</i>	Inner layer of shells (Nacre)	109.1	7.6	55
<i>Trochus niloticus</i>	Inner layer of shells (Nacre)	104.2	8	55
<i>Trochus niloticus</i>	Inner layer of shells (Nacre)	103.3	8.7	55
<i>Trochus niloticus</i>	Inner layer of shells (Nacre)	136.1	9.7	55
<i>Trochus niloticus</i>	Inner layer of shells (Nacre)	142.5	10.2	55
<i>Trochus niloticus</i>	Inner layer of shells (Nacre)	127.1	10.3	55
<i>Trochus niloticus</i>	Inner layer of shells (Nacre)	118	10.6	55
<i>Trochus niloticus</i>	Inner layer of shells (Nacre)	119.1	11.4	55
<i>Trochus niloticus</i>	Inner layer of shells (Nacre)	113.3	10.8	55
<i>Haliotis rufescens</i>	Nacrous layer	36.5	1.13	68
<i>Ensis siliqua</i>	Shell	82.4	3.86	56
<i>Crassostrea gigas</i>	Folia	73	3.2	57
<i>Harpisquilla harpax</i>	Spearer	34.03	1.33	58
<i>Odontodactylus scyllarus</i>	Smasher	34.03	1.39	58
<i>Harpisquilla harpax</i>	Spearer	4.55	0.06	58
<i>Odontodactylus scyllarus</i>	Smasher	5.63	0.07	58

Table II. continued

Species	Part	E (GPa)	H (GPa)	Ref
<i>Harpiosquilla harpax</i>	Spearer	9.87	0.36	58
<i>Odontodactylus scyllarus</i>	Smasher	9.61	0.29	58
<i>Harpiosquilla harpax</i>	Spearer	0.96	0.04	58
<i>Odontodactylus scyllarus</i>	Smasher	0.87	0.03	58
<i>Paracentrotus lividus</i>	Spine (septa transverse)	58.57	3.84	59
<i>Paracentrotus lividus</i>	Spine (central strereom transverse)	32.2	1.76	59
<i>Paracentrotus lividus</i>	Spine (septa longitudinal at milled ring)	65.5	2.71	59
<i>Paracentrotus lividus</i>	Spine (transverse bridges)	25.86	0.69	59
<i>Paracentrotus lividus</i>	Spine (septa longitudinal at midshaft)	64.47	2.73	59
<i>Pectinidae</i>	Shell	88.2	5	60
<i>Limacina helicina antarctica</i>	Shell	45.27	2.3	61
<i>Cavolinia uncinata</i>	Shell	85.9	5.2	62
<i>Cavolinia uncinata</i>	Shell	51.5	5.6	62
<i>Isursus oxyrinchus</i>	Tooth, axial	99	6.2	63
<i>Isursus oxyrinchus</i>	Tooth, axial, tip	131	7.5	63
<i>Isursus oxyrinchus</i>	Tooth, transversal	127	6.8	63
<i>Galeocerdo cuvier</i>	Tooth, axial	98	6	63
<i>Galeocerdo cuvier</i>	Tooth, axial, tip	94	5.8	63
<i>Galeocerdo cuvier</i>	Tooth, transversal	100	6.1	63
Human	Wisdom tooth, axial	109	7	63
Human	Wisdom tooth, axial, tip	116	7.6	63
Human	Wisdom tooth, transversal	106	6.3	63
<i>Trochus maculatus</i>	Shell	85	6.52	64
<i>Haliotis rufescens</i>	Shell	75	5.82	64
<i>Pteria penguin</i>	Shell	63	3.73	64
<i>Meretrix lusoria</i>	Shell	64	2.71	64
<i>Pecten maximus</i>	Shell	86	3.27	64
Mice	Tibiae	20.01	0.74	65
Mice	Tibiae	11.5	0.23	65
<i>Monorhaphis chuni</i>	Spicule	38.68	4.01	67
<i>Monorhaphis chuni</i>	Spicule	42.94	4.53	67
<i>Physeter macrocephalus</i>	Skull	11.36	0.4	66
<i>Physeter macrocephalus</i>	Skull	13.11	0.5	66
<i>Physeter macrocephalus</i>	Skull	12.15	0.44	66

Table III. Elastic modulus (E) and hardness (H) of ultrafine-grained (UFG) ceramic and metallic materials, as shown in Fig. 3a, b

Material	Grain size (nm)	E (GPa)	H (GPa)	Ref
ZrO ₂ -3 wt.% Y ₂ O ₃ (Y-TZP)	23	171	7.96	72
ZrO ₂ -3 wt.% Y ₂ O ₃ (Y-TZP)	35	188	6.24	72
ZrO ₂ -3 wt.% Y ₂ O ₃ (Y-TZP)	43	186	6.23	72
ZrO ₂ -3 wt.% Y ₂ O ₃ (Y-TZP)	45	210	6.21	70
Ni-P	4.1	178	7.81	74
Ni-P	7.1	188	8.33	74
Ni-P	17.1	195	6.72	74
Ni-P	28.9	205	6.05	74
Y ₃ Al ₅ O ₁₂ (YAG)	60	212	15	75
Si	8	199	11.9	76
Si	25	203	11.8	76
ZnO	7.4	44.8	1.896	77
ZnO	24	56.94	2.994	77
TiO ₂	12.2	56.19	1.34	87
TiO ₂	14.3	127.94	4.57	87
TiO ₂	32.4	175.56	6.9	87
Ta-W thin film	35.9	181.73	14.29	79

Table III. continued

Material	Grain size (nm)	E (GPa)	H (GPa)	Ref
WC-10 wt.% Co	61	596.28	28.95	80
Al ₂ O ₃ (2-5 nm) /a-Al ₂ O ₃ composite coating		195	10	81
ZrC film	7.7	218.8	29.33	83
ZrC film	9.7	220.63	25.29	83
ZrC film	9.7	242.15	24.75	83
ZrC film	12.9	270.85	17.76	83
β -Ti alloy	10	43.3	3.39	70
Ni-alloy	13	200	6.2	71
AA8006 alloy	200	31.4	1.62	73
AA8006-B ₄ C nanostructured nanocomposite	35	67.4	2.15	73
Ni	81	203	4.1	82
Ni	44	204	5	82
Ni	37	194	5.3	82
Ni	23	209	6.3	82
Ni-Fe 7.3% wt	32	202	5.6	82
Ni-Fe 16% wt	12	189	6.5	82
Ni-Fe 23% wt	10	187	6.4	82
Ni-Fe 32% wt	9.8	169	6.3	82
Cu	59	100	1.9	84
Ni	56.5	206	3	84
Au-ZnO (1% vol)	77	82.2	2.23	85
Au-ZnO (1% vol)	71	82.5	2.46	85
Ti RD-TD	80	122	3.8	86
Ti ND-RD	80	119.85	3.65	86
Ti TD-ND	80	109.93	3.44	86
Ti RD-TD	130	124.94	3.51	86
Ti ND-RD	130	121.03	3.29	86
Ti TD-ND	130	115.45	3.18	86

Table IV. Elastic modulus (E) and hardness (H) of FCC single crystals, as shown in Fig. 4

Material	E (GPa)	H (GPa)	Ref
Cu (100)	108	1.1	37
Ni (001)	247.59	1.24	38
Ag (001)	91.86	0.71	38
Au (001)	86.34	1.02	37
Fe-15Cr-15Ni	156	1.46	88
Fe-30Ni	136	1.43	88
Al (100)	73.6	0.256	36
Al (110)	75.5	0.2696	36
Al (111)	76.9	0.2616	36

The elastic moduli of Ni (001)/Ag (001)/Au (001) were obtained from the respective shear modulus, as $E = 2(1+\nu)*G$.

Table V. Elastic modulus (E) and hardness (H) of bulk metallic glasses and amorphous silicon, as shown in Fig. 5.

Material	E (GPa)	H (GPa)	Ref
Fe ₄₁ Co ₇ Cr ₁₅ Mo ₁₄ C ₁₅ B ₆ Y ₂	226	12.57	89
Ni ₅₀ Nb ₅₀	132	8.93	90
Ni ₄₀ Cu ₅ Ti ₁₇ Zr ₂₈ Al ₁₀	133.9	8.45	91
Ni _{39.8} Cu _{5.97} Ti _{15.92} Zr _{27.86} Al _{9.95} Si _{0.5}	117	8.13	91
Ni ₄₀ Cu ₅ Ti _{16.5} Zr _{28.5} Al ₁₀	122	7.84	91
Ni ₄₅ Ti ₂₀ Zr ₂₅ Al ₁₀	114	7.76	91
Ni ₄₀ Cu ₆ Ti ₁₆ Zr ₂₈ Al ₁₀	111	7.65	91
{Zr ₄₁ Ti ₁₄ Cu _{12.5} Ni ₁₀ Be _{22.5} } ₉₈ Y ₂	107.6	6.76	92
Zr ₅₄ Al ₁₅ Ni ₁₀ Cu ₁₉ Y ₂	92.1	6.49	92
Zr ₅₃ Al ₁₄ Ni ₁₀ Cu ₁₉ Y ₄	86	6.44	92
Zr ₄₁ Ti ₁₄ Cu _{12.5} Ni ₈ Be _{22.5} C ₁	106	6.13	92
Zr _{46.75} Ti _{8.25} Cu _{7.5} Ni ₁₀ Be _{27.5}	100	6.1	90
Zr ₄₈ Nb ₈ Cu ₁₄ Ni ₁₂ Be ₁₈	93.7	6.09	92
Zr ₃₄ Ti ₁₅ Cu ₁₀ Ni ₁₁ Be ₂₈ Y ₂	109.8	6.07	92
Zr ₅₇ Nb ₅ Cu _{15.4} Ni _{12.6} Al ₁₀	87.3	5.9	90
Zr ₄₈ Nb ₈ Cu ₁₂ Fe ₈ Be ₂₄	95.7	5.85	92
Zr ₄₀ Ti ₁₅ Cu ₁₁ Ni ₁₁ Be _{21.5} Y ₁ Mg _{0.5}	94.2	5.74	92
Zr ₄₁ Ti ₁₄ Cu _{12.5} Ni ₁₀ Be _{22.5}	101	5.97	90, 92
Zr ₄₁ Ti ₁₄ Cu _{12.5} Ni ₁₀ Be _{22.5}	101	5.4	39, 90
Zr ₄₁ Ti ₁₄ Cu _{12.5} Ni ₁₀ Be _{22.5}	101	5.88	90, 94
Zr ₄₁ Ti ₁₄ Cu _{12.5} Ni ₁₀ Be _{22.5}	101	5.23	90
Zr ₆₅ Al ₁₀ Ni ₁₀ Cu ₁₅	83	5.6	90
Zr ₆₅ Al ₁₀ Ni ₁₀ Cu ₁₅	83	5.6	90
Zr ₅₇ Ti ₅ Cu ₂₀ Ni ₈ Al ₁₀	82	5.4	90
Cu ₆₀ Hf ₁₀ Zr ₂₀ Ti ₁₀	101	7	90
Cu ₅₀ Zr ₅₀	88.7	5.8	90
Cu ₅₀ Zr ₅₀	85	5.8	90
Cu ₅₀ Zr ₄₅ Al ₅	102	5.4	90
Pd ₄₀ Ni ₄₀ P ₂₀	108	5.38	90
Pd ₄₀ Ni ₄₀ P ₂₀	108	5.3	90
Pd ₄₀ Ni ₁₀ Cu ₃₀ P ₂₀	98	5	90
Pd _{77.5} Si _{16.5} Cu ₆	92.9	4.5	90
Pd _{77.5} Si _{16.5} Cu ₆	96	4.5	90
Pt ₆₀ Ni ₁₅ P ₂₅	96	4.1	90
Mg ₆₅ Cu ₂₅ Tb ₁₀	51.3	2.83	90
Nb ₆₀ Al ₁₀ Fe ₂₀ Co ₁₀	51.2	2.2	90
Ce ₇₀ Al ₁₀ Ni ₁₀ Cu ₁₀	30	1.5	90
Er ₅₅ Al ₂₅ Co ₂₀	70.72	5.45	93
Dy ₅₅ Al ₂₅ Co ₂₀	61.36	4.7	93
Tb ₅₅ Al ₂₅ Co ₂₀	59.53	4.42	93
Ho ₅₅ Al ₂₅ Co ₂₀	66.64	4.14	93
La ₅₅ Al ₂₅ Co ₂₀	40.9	3.48	93
La ₅₅ Al ₂₅ Cu ₁₀ Ni ₅ Co ₅	41.9	3	93
Pr ₅₅ Al ₂₅ Co ₂₀	45.9	2.58	93
a*-Si	179	11.3	76
a*-Si	167	11.1	76
a*-Si	173	11.6	76
a*-Si	152	10	76
a*-Si	140	9.6	76
a*-Si	140	8.8	76

a*: amorphous.

REFERENCES

1. M.A. Boles, M. Engel, and D.V. Talapin, *Chem. Rev.* 116, 11220. (2016).
2. E.V. Sturm and H. Cölfen, *Curr. Comput. Aided Drug Des.* 7, 207. (2017).
3. D. Giuntini, S. Zhao, T. Krekeler, M. Li, M. Blankenburg, B. Bor, G. Schaan, B. Domènech, M. Müller, I. Scheider, M. Ritter, and G.A. Schneider, *Sci. Adv.* 7(2), eabb6063. (2021).
4. M.R. Begley, D.S. Gianola, and T.R. Ray, *Science* 364, 1250. (2019).
5. D. Giuntini, E. Torresani, K.T. Chan, M. Blankenburg, L. Saviot, B. Bor, B. Domènech, M. Shachar, M. Müller, E.A. Olevsky, J.E. Garay, and G.A. Schneider, *Nanoscale Adv.* 1, 3139. (2019).
6. X.W. Gu, *JOM* 70, 2205. (2018).
7. M.P. Pileni, *EPL* 119, 37002. (2017).
8. E. Tam, P. Podsiadlo, E. Shevchenko, D.F. Ogletree, M.P. Delplancke-Ogletree, and P.D. Ashby, *Nano Lett.* 10, 2363. (2010).
9. P. Podsiadlo, G. Krylova, B. Lee, K. Critchley, D.J. Gosztola, D.V. Talapin, P.D. Ashby, and E.V. Shevchenko, *J. Am. Chem. Soc.* 132, 8953. (2010).
10. A. Dreyer, A. Feld, A. Kornowski, E.D. Yilmaz, H. Noei, A. Meyer, T. Krekeler, C. Jiao, A. Stierle, V. Abetz, H. Weller, and G.A. Schneider, *Nat. Mater.* 15, 522. (2016).
11. B. Bor, D. Giuntini, B. Domènech, M.V. Swain, and G.A. Schneider, *J. Eur. Ceram. Soc.* 39, 3247. (2019).
12. B. Domènech, A. Plunkett, M. Kampfbeck, M. Blankenburg, B. Bor, D. Giuntini, T. Krekeler, M. Wagstaffe, H. Noei, A. Stierle, M. Ritter, M. Müller, T. Vossmeier, H. Weller, and G.A. Schneider, *Langmuir* 35, 13893. (2019).
13. M. Li, I. Scheider, B. Bor, B. Domènech, G.A. Schneider, and D. Giuntini, *Compos. Sci. Technol.* 198, 108283. (2020).
14. B. Domènech, A.T.L. Tan, H. Jelitto, E.Z. Berodt, M. Blankenburg, O. Focke, J. Cann, C.C. Tazan, L.C. Ciacchi, M. Müller, K.P. Furlan, A.J. Hart, and G.A. Schneider, *Adv. Eng. Mater.* 22, 2000352. (2020).
15. D. Giuntini, A. Davydok, M. Blankenburg, B. Domènech, B. Bor, M. Li, I. Scheider, C. Krywka, M. Müller, and G.A. Schneider, *Nano Lett.* 21, 2891. (2021).
16. B. Bor, D. Giuntini, B. Domènech, A. Plunkett, M. Kampfbeck, T. Vossmeier, H. Weller, I. Scheider, and G.A. Schneider, *Appl. Phys. Rev.* 8, 031414. (2021).
17. C.A. Schuh, *Mater. Today* 9, 32. (2006).
18. W.C. Oliver and G.M. Pharr, *J. Mater. Res.* 7, 1564. (1992).
19. P.J. Santos, P.A. Gabrys, L.Z. Zornberg, M.S. Lee, and R.J. Macfarlane, *Nature* 591, 586. (2021).
20. B. Merle, V. Maier-Kiener, and G.M. Pharr, *Acta Mater.* 134, 167. (2017).
21. G.M. Pharr, J.H. Strader, and W.C. Oliver, *J. Mater. Res.* 24, 653. (2009).
22. X.Q. Chen, H. Niu, D. Li, and Y. Li, *Intermetallics* 19, 1275. (2011).
23. Y.T. Cheng and C.M. Cheng, *Appl. Phys. Lett.* 73, 614. (1998).
24. R. Yang, T. Zhang, P. Jiang, and Y. Bai, *Appl. Phys. Lett.* 92, 231906. (2008).
25. D.M. Teter, *MRS Bull.* 23, 22. (1998).
26. K. Durst, O. Franke, A. Böhner, and M. Göken, *Acta Mater.* 55, 6825. (2007).
27. P. Stempfle, O. Pantalé, M. Rousseau, E. Lopez, and X. Bourrat, *Mater. Sci. Eng. C* 30, 715. (2010).
28. C. Wang and C.C. Sun, *Cryst. Eng. Comm.* 22, 1149. (2020).
29. J.J. Gilman, *Science* 261, 1436. (1993).
30. D. Labonte, A.K. Lenz, and M.L. Oyen, *Acta Biomater.* 57, 373. (2017).
31. X. Qin, D. Luo, Z. Xue, Q. Song, and T. Wang, *Adv. Mater.* 30, 1706327. (2018).
32. M. Gauvin, Y. Wan, I. Arfaoui, and M.P. Pileni, *J. Phys. Chem. C* 118, 5005. (2014).
33. K.S. Sugi, P. Bandyopadhyay, M. Bodiuzzaman, A. Nag, M. Hridya, W.A. Dar, P. Ghosh, and T. Pradeep, *Chem. Mater.* 32, 7973. (2020).
34. A. Bokov, S. Zhang, L. Feng, S.J. Dillon, R. Faller, and R.H.R. Castro, *J. Eur. Ceram. Soc.* 38, 4260. (2018).
35. A.H. Chokshi, A. Rosen, J. Karch, and H. Gleiter, *Scr. Metall.* 23, 1679. (1989).
36. P. Filippov and U. Koch, *Materials* 12, 3688. (2019).
37. R. Bolin, H. Yavas, H. Song, K.J. Hemker, and S. Papanikolaou, *Curr. Comput. Aided Drug Des.* 9, 652. (2019).
38. Z. Zong, J. Lou, O.O. Adewoye, A.A. Elmustafa, F. Hammad, and W.O. Soboyejo, *Mater. Manuf. Process.* 22, 228. (2007).
39. W.H. Wang and H.Y. Bai, *Mater. Lett.* 44, 59. (2000).
40. R.O. Ritchie, *Nat. Mater.* 10, 817. (2011).
41. B. Domènech, M. Kampfbeck, E. Larsson, T. Krekeler, B. Bor, D. Giuntini, M. Blankenburg, M. Ritter, M. Müller, T. Vossmeier, H. Weller, and G.A. Schneider, *Sci. Rep.* 9, 3435. (2019).
42. B. Bor, L. Heilmann, B. Domènech, M. Kampfbeck, T. Vossmeier, H. Weller, G.A. Schneider, and D. Giuntini, *Molecules* 25, 4790. (2020).
43. J.Y. Sun and J. Tong, *J. Bionic Eng.* 4, 11. (2007).
44. S. Bentov, P. Zaslansky, A.A. Sawalmih, A. Masic, P. Fratzl, A. Sagi, A. Berman, and B. Aichmayer, *Nat. Commun.* 3, 839. (2012).
45. L.B. Whitenack, D.C. Simkins, P.J. Motta, M. Hirai, and A. Kumar, *Arch. Oral Biol.* 55, 203. (2010).
46. A.J. Goetz, E. Griesshaber, R. Abel, T. Fehr, B. Ruthensteiner, and W.W. Schmahl, *Acta Biomater.* 10, 3885. (2014).
47. J. Lv, Y. Jiang and D. Zhang, *J. Bionic Eng.* 12, 276. (2015).
48. T. Schöberl and I.L. Jäger, *Adv. Eng. Mater.* 8, 1164. (2006).
49. D. Losic, K. Short, J.G. Mitchell, R. Lal, and N.H. Voelcker, *Langmuir* 23, 5014. (2007).
50. A.P. Huerta, M. Cusack, W. Zhu, J. England, J. Hughes, and J.R. Soc, *Interface* 4, 33. (2007).
51. J.C. Weaver, Q. Wang, A. Miserez, A. Tantuccio, R. Stromberg, K.N. Bozhilov, P. Maxwell, R. Nay, S.T. Heier, E. Di-Masi, and D. Kisailus, *Mater. Today* 13, 42. (2010).
52. P.Y. Chen, J. Schirer, A. Simpson, R. Nay, Y.S. Lin, W. Yang, M.I. Lopez, J. Li, E.A. Olevsky, and M.A. Meyers, *J. Mater. Res.* 27, 100. (2012).
53. C. Merkel, J. Deuschle, E. Griesshaber, S. Enders, E. Steinhauser, R. Hochleitner, U. Brand, and W.W. Schmahl, *J. Struct. Biol.* 168, 396. (2009).
54. Y.S. Lin, C.T. Wei, E.A. Olevsky, and M.A. Meyers, *J. Mech. Behav. Biomed. Mater.* 4, 1145. (2011).
55. B.J.F. Bruet, H.J. Qi, M.C. Boyce, R. Panas, K. Tai, L. Frick, and C. Ortiz, *J. Mater. Res.* 20, 2400. (2005).
56. D.J. Scurr and S.J. Eichhorn, *J. Mater. Res.* 21, 3099. (2006).
57. S.W. Lee, G.H. Kim, and C.S. Choi, *Mater. Sci. Eng. C* 28, 258. (2008).
58. M. Tadayon, S. Amini, A. Masic, and A. Miserez, *Adv. Funct. Mater.* 25, 6437. (2015).
59. C. Moureaux, A. Pérez-Huerta, P. Compère, W. Zhu, T. Leloup, M. Cusack, and P. Dubois, *J. Struct. Biol.* 170, 41. (2010).
60. X. Li and P. Nardi, *Nanotechnology* 15, 211. (2004).
61. C.M.H. Teniswood, D. Roberts, W.R. Howard, and J.E. Bradby, *ICES J. Mar. Sci.* 70, 1499. (2013).
62. T. Zhang, Y. Ma, K. Chen, M. Kunz, N. Tamura, M. Qiang, J. Xu, and L. Qi, *Angew. Chem.* 123, 10545. (2011).
63. J. Enax, O. Prymak, D. Raabe, and M. Epple, *J. Struct. Biol.* 178, 290. (2012).
64. F.D. Fleischli, M. Dietiker, C. Borgia, and R. Spolenak, *Acta Biomater.* 4, 1694. (2008).
65. N.R. Florez, M.L. Oyen, and S.J. Shefelbine, *J. Mech. Behav. Biomed. Mater.* 18, 90. (2013).
66. P. Alam, S. Amini, M. Tadayon, A. Miserez, and A. Chinsamy, *Zoology* 119, 42. (2016).
67. A. Miserez, T. Schneberk, C.J. Sun, F.W. Zok, and J.H. Waite, *Science* 319, 1816. (2008).
68. F. Barthelat, C.M. Li, C. Comi, and H.D. Espinosa, *J. Mater. Res.* 21, 1977. (2006).
69. L. Romana, P. Thomas, P. Bilas, J.L. Mansot, M. Merrifields, Y. Bercion, and D.A. Aranda, *Mater. Character.* 76, 55. (2013).

70. K.Y. Xie, Y. Wang, Y. Zhao, L. Chang, G. Wang, Z. Chen, Y. Cao, X. Liao, E.J. Lavernia, R.Z. Valiev, B. Sarrafpour, H. Zoellner, and S.P. Ringer, *Mater. Sci. Eng. C* 33, 3530. (2013).
71. M. Baghbanan, U. Erb, and G. Palumbo, *Phys. Stat. Sol. A* 203, 1259. (2006).
72. R. Chaim and M. Hefetz, *J. Mater. Sci.* 39, 3057. (2004).
73. F. Khodabakhshi, A.P. Gerlich, D. Verma, and M. Haghshenas, *Mater. Sci. Eng. A* 744, 120. (2019).
74. Y. Zhou, U. Erb, K.T. Aust, and G. Palumbo, *Scr. Mater.* 48, 825. (2003).
75. H.M. Wang, Z.Y. Huang, J.S. Jiang, K. Liu, M.Y. Duan, Z.W. Lu, J. Cedelle, Z.W. Guan, T.C. Lu, and Q.Y. Wang, *Mater. Des.* 105, 9. (2016).
76. V. Kulikovskiy, V. Vorlíček, P. Boháč, M. Stranyánek, R. Ctvrtlík, A. Kurdyumov, and L. Jastrabík, *Surf. Coat. Technol.* 202, 1738. (2008).
77. M.J. Mayo, R.W. Siegeland, Y.X. Liao, and W.D. Nix, *J. Mater. Res.* 7, 973. (1992).
78. G. Guisbiers, E. Herth, L. Buchailot, and T. Pardoën, *Appl. Phys. Lett.* 97, 143115. (2010).
79. C.L. Wang, M. Zhang, J.P. Chu, and T.G. Nieh, *Scr. Mater.* 58, 195. (2008).
80. Y. Peng, H. Wang, C. Zhao, H. Hu, X. Liu, and X. Song, *Compos. Part B* 197, 108161. (2020).
81. F.G. Ferré, E. Bertarelli, A. Chiodoni, D. Carnelli, D. Gastaldi, P. Vena, M.G. Beghi, and F. di Fonzo, *Acta Mater.* 61, 2662. (2013).
82. J.D. Giallonardo, U. Erb, K.T. Aust, and G. Palumbo, *Philos. Mag.* 91, 4594. (2011).
83. C.S. Chen, C.P. Liu, and C.Y.A. Tsao, *Thin Solid Films* 479, 130. (2005).
84. S. Bansal, A. Saxena, T. Hartwig, and R.R. Tummala, *J. Metastable Nanocryst. Mater.* 23, 183. (2005).
85. N. Argibay, J.E. Mogonye, J.R. Michael, R.S. Goeke, P.G. Kotula, T.W. Scharf, M.T. Dugger, and S.V. Prasad, *J. Appl. Phys.* 117, 145302. (2015).
86. Z. Li, L. Fu, B. Fu, X. Yang, and A. Shan, *J. Nanosci. Nanotechnol.* 14, 7740. (2014).
87. M.J. Mayo, R.W. Siegel, A. Narayanasamy, and W.D. Nix, *J. Mater. Res.* 5, 1073. (1990).
88. Y.Z. Xia, H. Bei, Y.F. Gao, D. Catoor, and E.P. George, *Mater. Sci. Eng. A* 611, 177. (2014).
89. V. Keryvin, V.H. Hoang, and J. Shen, *Intermetallics* 17, 211. (2009).
90. W.H. Wang, *J. Appl. Phys.* 99, 093506. (2006).
91. D. Xu, G. Duan, W.L. Johnson, and C. Garland, *Acta Mater.* 52, 3493. (2004).
92. Y. Zhang, D.Q. Zhao, M.X. Pan, W.H. Wang, and J. Non-Cryst, *Solids* 315, 206. (2003).
93. S. Li, R.J. Wang, M.X. Pan, D.Q. Zhao, W.H. Wang, and J. Non-Cryst, *Solids* 354, 1080. (2008).
94. R.L. Narayan, K. Boopathy, I. Sen, D.C. Hofmann, and U. Ramamurty, *Scr. Mater.* 63, 768. (2010).
95. U.G.K. Wegst, H. Bai, E. Saiz, A.P. Tomsia, and R.O. Ritchie, *Nat. Mater.* 14, 23. (2015).

Publisher's Note Springer Nature remains neutral with regard to jurisdictional claims in published maps and institutional affiliations.